

SCIENTIFIC REPORTS



OPEN

High-internal-phase emulsions stabilized by metal-organic frameworks and derivation of ultralight metal-organic aerogels

Received: 11 November 2015

Accepted: 22 January 2016

Published: 19 February 2016

Bingxing Zhang, Jianling Zhang, Chengcheng Liu, Li Peng, Xinxin Sang, Buxing Han, Xue Ma, Tian Luo, Xiuniang Tan & Guanying Yang

To design high-internal-phase emulsion (HIPE) systems is of great interest from the viewpoints of both fundamental researches and practical applications. Here we demonstrate for the first time the utilization of metal-organic framework (MOF) for HIPE formation. By stirring the mixture of water, oil and MOF at room temperature, the HIPE stabilized by the assembly of MOF nanocrystals at oil-water interface could be formed. The MOF-stabilized HIPE provides a novel route to produce highly porous metal-organic aerogel (MOA) monolith. After removing the liquids from the MOF-stabilized HIPE, the ultralight MOA with density as low as $0.01 \text{ g}\cdot\text{cm}^{-3}$ was obtained. The HIPE approach for MOA formation has unique advantages and is versatile in producing different kinds of ultralight MOAs with tunable porosities and structures.

Metal-organic frameworks (MOFs) are crystalline materials that are composed of metal ions or clusters bridged by organic ligands^{1–3}. Recently, numerous efforts have been devoted to the design of MOFs with macro- or mesoporous three-dimensional (3D) architectures due to their wide applications in different fields such as gas storage^{4–7}, gas separation^{8–10}, chemical sensing^{11–14} and catalysis^{15–19}. Among the diverse kinds of MOF architectures, the metal-organic aerogel (MOA) has emerged as a new porous material, which is expected not only to preserve the intrinsic pore volume of MOF in an integral material but also to permit the efficient practical applications due to their easy-handling shape^{20–23}. The MOA is generally derived from a metal-organic gel (MOG) matrix^{20–23}. Nevertheless, the formation of MOG driven by metal-ligand coordination is often difficult because precipitation or crystallization occurs frequently²⁴.

High-internal-phase emulsion (HIPE), which is also known as concentrated emulsion or gel emulsion, is emulsion that its internal phase has a high volume fraction. Because the high-content internal phase is tightly packed by the continuous phase which forms persistent microscopic liquid films, HIPE is highly viscous. Up to now, HIPEs have found wide applications in polymerization^{25,26}, material synthesis^{27,28}, etc. In general, surfactants are used to emulsify the immiscible solvents (water and oil) for HIPE formation^{25–29}. Recently, there have been increasing interests in utilizing solid particles as emulsifiers for the preparation of HIPEs^{30–32}. The particles for stabilizing HIPE are organic or inorganic particles and the functionalization for the solid particles is usually needed to modify the amphiphilicity of particles (e.g. functionalized silica and surface-active polymers particles). Moreover, the additional additives (e.g. salt, acid, etc) and high-energy input (e.g. high shear force or high speed homogenization) are requisite for producing HIPE. To design simple HIPE systems stabilized by solid particles are of great interest, but still remain challenging.

Owing to the hybrid composition, mid-range zeta potentials and tunable structures, MOF crystallites can assemble at liquid-liquid interface^{33,34}. Here we demonstrate for the first time the utilization of MOF for HIPE formation. It was found that the HIPE could be prepared by stirring the mixture of water, oil and MOF at room temperature, involving no additional additives or high-energy input. The MOF nanocrystals assembled at oil-water interface play an exceptional role in stabilising the HIPE. Such a MOF-stabilized HIPE with high viscosity and large internal phase volume fraction (>0.7) makes it possible to produce highly porous MOA monolith.

Beijing National Laboratory for Molecular Sciences, CAS Key Laboratory of Colloid and Interface and Thermodynamics, Institute of Chemistry, Chinese Academy of Sciences, Zhongguancun North First Street 2, Beijing 100190, China. Correspondence and requests for materials should be addressed to J.Z. (email: zhangjl@iccas.ac.cn)

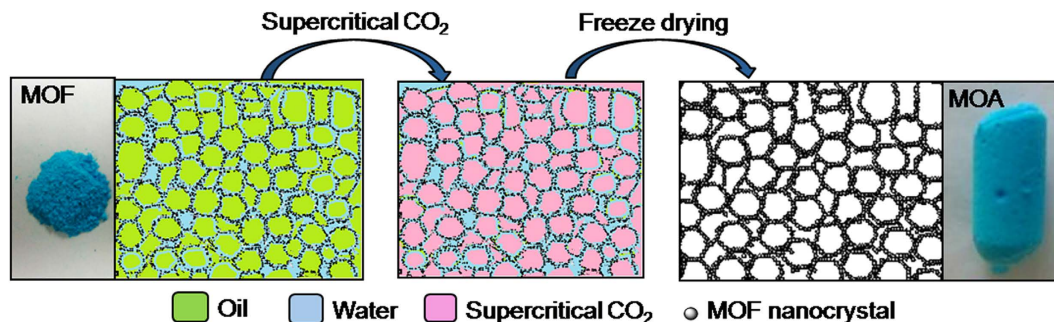


Figure 1. Diagram illustrating the MOF-stabilized HIPE and derivation of MOA from HIPE.

A strategy for deriving MOA from the MOF-stabilized HIPE is proposed, as illustrated in Fig. 1. The HIPE stabilized by the assembly of pre-formed MOF nanoparticles at oil-water interface is first prepared. Then the inner oil phase and outer water phase are subsequently removed by supercritical CO₂ replacement and freeze drying. The MOA that preserves the skeleton replica of HIPE can be thus obtained. This approach for MOA formation has unique advantages. Since the HIPE contains only three components, i.e. solid MOF and two liquids (water and oil), pure MOA solid can be easily obtained by removing the liquids and the complicated post-processing (such as washing and separating) suffering from the conventional HIPE is avoided. The route is versatile in producing different kinds of ultralight MOAs with tunable porosities and structures.

Results

Diethyl ether-in-water HIPE stabilized by Cu₃(BTC)₂. Cu₃(BTC)₂ (BTC = 1,3,5-benzenetricarboxylate) is one of the most widely studied MOFs and has diverse applications in different fields^{35–40}. Here Cu₃(BTC)₂⁴¹ was used as a stabilizer for HIPE. The concentration of Cu₃(BTC)₂ was fixed at 10 mg·mL⁻¹ of the overall volume of water and diethyl ether. For a typical synthesis, the mixture of water, diethyl ether and Cu₃(BTC)₂ was stirred 3 hrs at room temperature for emulsification. Then the stir was stopped and the emulsion completely separated into two phases in 8 hrs. As the diethyl ether volume fraction was in the range of 0.29~0.57, the emulsion separated into a lower phase of excess water and an upper emulsion (Fig. 2a–c). Interestingly, the upper emulsion presented gel-like or semi-solid appearance, which is a key character for the HIPE formation. The composition of the upper HIPE was calculated by subtracting the lower water. The diethyl ether volume fractions of the three HIPEs, formed from the emulsions with the initial diethyl ether volume fractions of 0.57, 0.43 and 0.29, are 0.78, 0.75 and 0.73, while the MOF concentrations are 1.5 wt%, 2.0 wt% and 2.8 wt%, respectively. Outside the diethyl ether volume fraction range of 0.29~0.57, the gel emulsion cannot form (Supplementary Fig. 1).

The microstructures of the HIPEs were characterized by confocal laser scanning microscopy (CLSM). To identify each phase in the HIPE, the water phase was marked by Rhodamine B. The droplets are polyhedral and squeeze among each other, which are bridged by Cu₃(BTC)₂ nanoparticles (Fig. 2d–f). This morphology is characteristic of HIPE formation, being the best geometric conformation to achieve the most dense and optimized close-packed structure^{42–45}. The colorized CLSM images reveal that the HIPE is diethyl ether-in-water type. Namely, diethyl ether makes up the droplet, while water is the continuous phase. The average droplet sizes are 18 μm, 8 μm and 5 μm for the three HIPEs shown in Fig. 2d–f, respectively. Evidently, the droplet size decreases with the decreasing initial diethyl ether volume fraction of the emulsion. It is worth noting that the HIPE stabilized by Cu₃(BTC)₂ is very stable and can keep stability more than one month, which was confirmed by direct observation and CLSM images (Supplementary Fig. 2).

Cu₃(BTC)₂ MOAs derived from HIPEs. The very high viscosity and large internal phase of the above HIPEs at low MOF concentration (<3.0 wt%) endow them unique advantage for forming intact and highly porous MOA monoliths. Solvent removal is a key step to preserve the porous structure and the monolith shape. The diethyl ether inside the droplet was firstly replaced by supercritical CO₂ to keep the monolithic shape of original HIPE. CO₂ was then released under frozen state and water was removed by lyophilization. The as-synthesized MOA presents an aerogel appearance with an outstanding volume expansion (Fig. 3b) compared with the pristine Cu₃(BTC)₂ (Fig. 3a). The density of the MOA was determined to be 0.015 g·cm⁻³. Figure 3c shows that the X-ray diffraction (XRD) patterns of the pristine Cu₃(BTC)₂ and the MOAs synthesized from different HIPEs are nearly identical. It indicates that the MOAs preserve the crystal form of the pristine Cu₃(BTC)₂. No obvious difference was observed for the FT-IR spectra of the MOAs and the pristine Cu₃(BTC)₂ (Supplementary Fig. 3).

The scanning electron microscopy (SEM) images of the MOAs show the formation of macroporous structure (Fig. 3e–g), completely different from the morphologies of the pristine Cu₃(BTC)₂ (Fig. 3d). By combination with Fig. 2d–f, it can be seen that the MOAs well duplicate the respective microstructures of the HIPEs. From Fig. 3e–g, the macropore size of the MOA derived from HIPEs decreases with the decreasing initial diethyl ether volume fraction of the emulsion, in accordance with the decreased size of microdroplets in the HIPEs with different diethyl ether content (Fig. 2d–f). From the magnified SEM images shown in the inset of Fig. 3d, the pristine Cu₃(BTC)₂ presents particle aggregates in range of 20~80 nm. However, the nanoparticles are interconnected for the MOAs to form nanopores in dozens of nanometers (insets of Fig. 3e–g). The results prove that the pre-formed Cu₃(BTC)₂ nanoparticles can be reconstructed by HIPE.

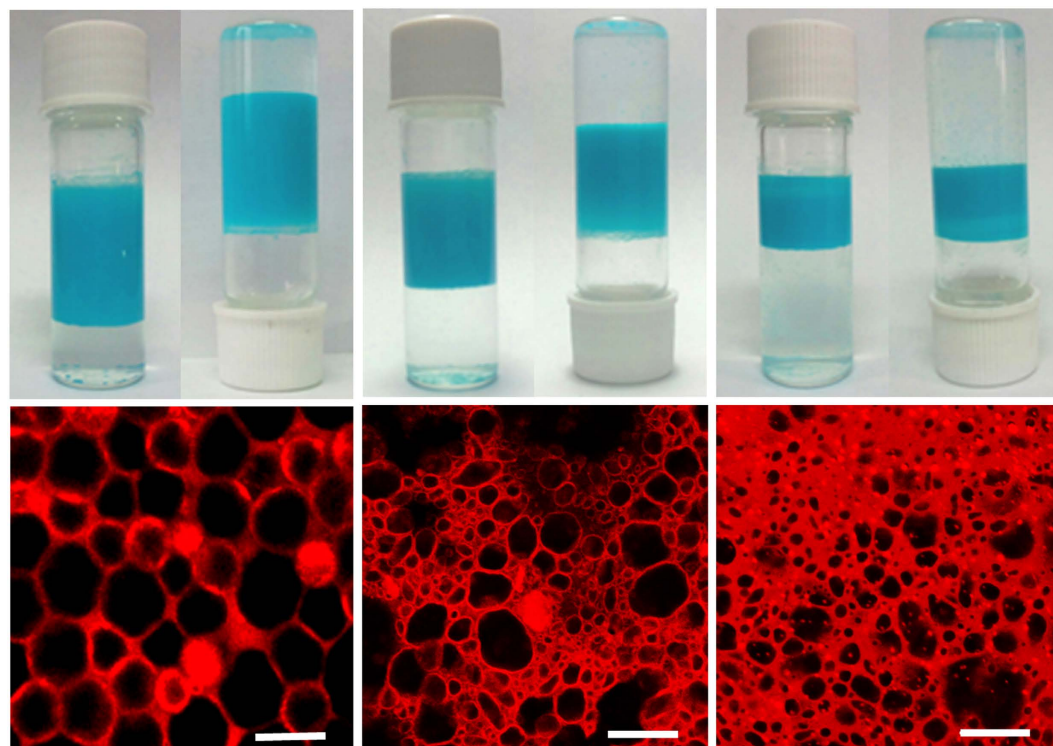


Figure 2. Characterization of $\text{Cu}_3(\text{BTC})_2$ -stabilized HIPEs. (a–c) Photographs of the emulsions stabilized by $\text{Cu}_3(\text{BTC})_2$ with the initial diethyl ether volume fractions of 0.57, 0.43 and 0.29, respectively. (d–f) The corresponding CLSM images of the above HIPEs (HIPE-1, HIPE-2 and HIPE-3, respectively). Scale bars, $20\ \mu\text{m}$.

Porosity and mechanical properties of $\text{Cu}_3(\text{BTC})_2$ MOAs. The macroporosities of the MOAs were determined by mercury porosimetry method after the sample was dried and degassed at $80\ ^\circ\text{C}$. As listed in Table 1, both the total macropore volume and porosity of the MOAs greatly increase compared with those of the pristine $\text{Cu}_3(\text{BTC})_2$. For example, the total macropore volume of the MOA synthesized in HIPE with initial diethyl ether volume fraction of 0.57 can reach $9.0\ \text{cm}^3\cdot\text{g}^{-1}$, much higher than that of the pristine MOF ($2.0\ \text{cm}^3\cdot\text{g}^{-1}$). The porosity degrees of the three MOAs are higher than 87%. Interestingly, the degree of porosity of the MOA is higher than the volume fraction of diethyl ether in the HIPE ($\sim 75\ \text{vol}\%$ internal phase). The excess porosity higher than the volume fraction of diethyl ether can be attributed to the nanopores formed by the interconnected $\text{Cu}_3(\text{BTC})_2$ particles, as shown in the insets of Fig. 3e–g. Moreover, it can be seen from Table 1 that the total macropore volumes and porosities of the three MOAs decrease with the decreasing initial diethyl ether volume fraction, accompanied with the increased density. It can be attributed to the decreased diethyl ether volume in the HIPE, because the diethyl ether droplets work as the templates for macropore formation. The macropore size distribution curves of the three MOAs are shown in Supplementary Fig. 4. All these curves show a bimodal size distribution, i.e. the macropores in microns with a high polydispersity and the nanopores smaller than $100\ \text{nm}$. As listed in Table 1, both the sizes of macropores and nanopores decrease with the decreasing initial diethyl ether volume fraction, which is consistent with that observed from the SEM images. The BET (Brunauer, Emmett and Teller) surface areas (S_{BET}) of the MOAs are higher than that of the pristine $\text{Cu}_3(\text{BTC})_2$ and increase with the decreased density (Table 1, Supplementary Fig. 5). The above results prove that the MOAs have hierarchically macro- and nanoporous architectures and their porosities can be easily modulated.

The mechanical properties of the $\text{Cu}_3(\text{BTC})_2$ MOA monoliths were measured by uniaxial compression (see photographs of compression test and stress-strain curves in Supplementary Fig. 6). The Young's modulus of the MOA is enhanced from $16\ \text{KPa}$ to $34\ \text{KPa}$ with the increased density (Table 1). In comparison with the $\text{Cu}_3(\text{BTC})_2$ monolith prepared by powder-packing synthesis (with a Young's modulus of $442\ \text{KPa}$)⁴⁶ and the polyacrylamide-supported $\text{Cu}_3(\text{BTC})_2$ monolith (stress values $\sim 1.5\ \text{MPa}$ at catastrophic failure)⁴⁷, the Young's modulus and compressive strength of the as-synthesized $\text{Cu}_3(\text{BTC})_2$ MOAs are lower. It can be attributed to the extremely low densities of the as-synthesized MOAs and the absence of a secondary phase as support for MOF skeleton.

Adsorption performance of $\text{Cu}_3(\text{BTC})_2$ MOA. The hierarchical macro- and nanoporous 3D architecture of the as-synthesized MOA would promote the diffusion of guest molecules into the pores (and active sites) of the framework. Here the elimination of different dyes in aqueous solutions by $\text{Cu}_3(\text{BTC})_2$ MOA was tested. The MOA shows enhanced adsorption capability for methylene blue (MB) and Rhodamine B (RHB) than the pristine $\text{Cu}_3(\text{BTC})_2$ (Fig. 4a). 86% of MB can be adsorbed by MOA within 1.5 min, while only 48% of MB can be adsorbed

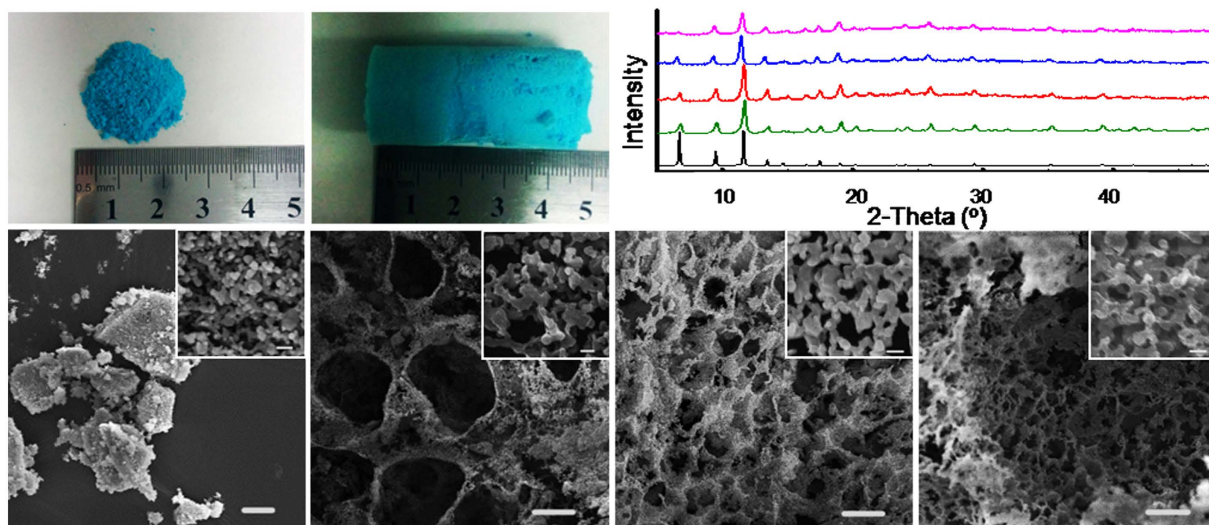


Figure 3. Characterization of the pristine $\text{Cu}_3(\text{BTC})_2$ and MOAs. (a,b) Photographs of the pristine $\text{Cu}_3(\text{BTC})_2$ and MOA-1 synthesized from HIPE-1; (c) Simulated XRD pattern of $\text{Cu}_3(\text{BTC})_2$ (black), XRD patterns of MOF (green), MOA-1 (red), MOA-2 (blue) and MOA-3 (pink) synthesized from HIPE-1, HIPE-2 and HIPE-3, respectively; (d-g) SEM images of the pristine $\text{Cu}_3(\text{BTC})_2$, MOA-1, MOA-2 and MOA-3. Scale bars, 10 μm in images (d-g) and 100 nm in the insets.

MOF/MOAs	Density ^a /g·cm ⁻³	Porosity ^b %	$V_{\text{pore}}^b/\text{cm}^3\cdot\text{g}^{-1}$	$D_{\text{macro}}^b/\mu\text{m}$	$D_{\text{nano}}^b/\text{nm}$	$S_{\text{BET}}^c/\text{m}^2\cdot\text{g}^{-1}$	Young's modulus/KPa
MOF	–	72.1	2.0	6.7	–	307	–
MOA-1	0.015	89.7	9.0	19.4	95	834	16
MOA-2	0.021	88.6	8.4	16.2	77	584	21
MOA-3	0.032	87.7	7.6	14.8	62	320	34

Table 1. Density, porosity and mechanical properties of the pristine $\text{Cu}_3(\text{BTC})_2$ and MOAs. ^adetermined by weighing method. ^bdetermined by mercury porosimetry method. ^cdetermined by N_2 adsorption-desorption method.

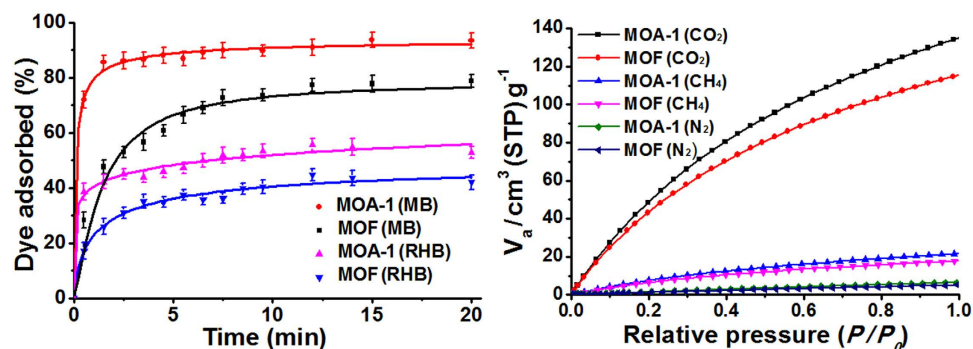


Figure 4. Adsorption performance of the pristine $\text{Cu}_3(\text{BTC})_2$ and MOA. (a) Kinetic adsorption curves of 10 mg MOA-1 (or the pristine $\text{Cu}_3(\text{BTC})_2$) in 10 mL of MB or RHB solutions (100 $\text{mg}\cdot\text{L}^{-1}$), respectively. (b) CO_2 , CH_4 and N_2 adsorption isotherms of the pristine $\text{Cu}_3(\text{BTC})_2$ and MOA-1 at 273.2 K.

by the pristine $\text{Cu}_3(\text{BTC})_2$. Upon adsorption equilibrium, the adsorption capacity (the adsorption amount of the dye per gram of the adsorbent) of MOA can reach 94.3 $\text{mg}\cdot\text{g}^{-1}$, higher than that of the pristine $\text{Cu}_3(\text{BTC})_2$ (78.2 $\text{mg}\cdot\text{g}^{-1}$). Also, the time taken to reach equilibrium is shortened by MOA (Fig. 4a). The adsorption capacity of the as-synthesized MOA is much higher than that of the reported Cr-BTC MOA over 1000 min at the same condition (20.2 $\text{mg}\cdot\text{g}^{-1}$)⁴⁸. The $\text{Cu}_3(\text{BTC})_2$ could be negatively charged under neutral condition and adsorb the positively charged dye cations through electrostatic attractions⁴⁹. Due to the highly porous structure of the $\text{Cu}_3(\text{BTC})_2$ MOA interconnected by nanoparticles, the transport limitation can be efficiently reduced, which is favorable for

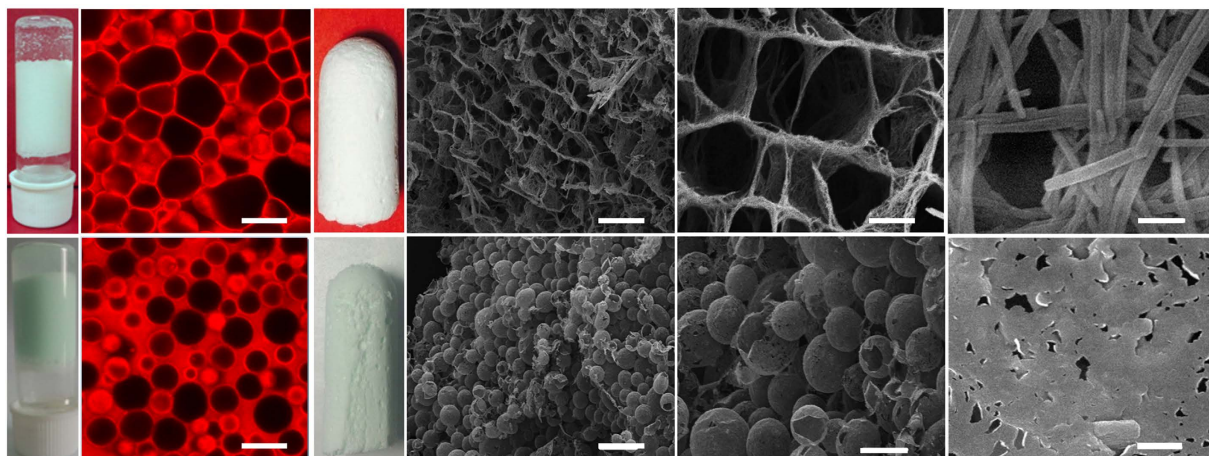


Figure 5. Characterization of the HIPEs stabilized by $Mn_3(BTC)_2$ and $Ni(BDC)$ and the corresponding MOAs. (a,b) Photograph and CLSM image of the HIPE stabilized by $Mn_3(BTC)_2$; (c–f) Photograph and SEM images of $Mn_3(BTC)_2$ MOA. (g,h) Photograph and CLSM image of the HIPE stabilized by $Ni(BDC)$; (i–l) Photograph and SEM images of $Ni(BDC)$ MOA. Scale bars, 20 μm (b,d,h,k), 10 μm (e), 50 μm (j) and 500 nm (f,l).

the accessibility to the active site of cationic charge. Therefore, the $Cu_3(BTC)_2$ MOA shows an enhanced adsorption capacity for MB molecules in aqueous solution. Further, the performance of the as-synthesized MOA for CO_2 capture was studied. At 1 atm, the CO_2 uptake for MOA-1 is $135 \text{ cm}^3 \cdot \text{g}^{-1}$ (Fig. 4b), which is a 17% increase than the pristine $Cu_3(BTC)_2$. In sharp contrast, the CO_2 uptake of the MOAs obtained from the gelation in pure ethanol at the same condition is less than $50 \text{ cm}^3 \cdot \text{g}^{-1}$ ²¹. From Fig. 4b, the MOA shows much lower adsorption for CH_4 and N_2 than CO_2 . It indicates that the MOA can be used as a promising candidate for the separation of CO_2/N_2 and CO_2/CH_4 with a high selectivity.

Cyclohexane-in-water HIPEs stabilized by $Cu_3(BTC)_2$. Cyclohexane was used as an alternative of diethyl ether to form MOF-stabilized HIPE with water. The results show that the cyclohexane-in-water HIPEs stabilized by $Cu_3(BTC)_2$ nanoparticles can be prepared (see photograph and CLSM image in Supplementary Fig. 7), similar to those of the diethyl ether-in-water HIPEs shown in Figs 1 and 2. The MOA monoliths were derived from the HIPEs after removing cyclohexane and water (Supplementary Fig. 7). The densities of the $Cu_3(BTC)_2$ MOAs obtained from HIPEs with the initial cyclohexane volume fractions of 0.57, 0.43 and 0.29 are $0.0096 \text{ g} \cdot \text{cm}^{-3}$, $0.014 \text{ g} \cdot \text{cm}^{-3}$ and $0.028 \text{ g} \cdot \text{cm}^{-3}$, respectively. The MOAs well preserve the crystal form of the pristine $Cu_3(BTC)_2$ (see XRD patterns in Supplementary Fig. 7).

HIPEs stabilized by $Mn_3(BTC)_2$ and $Ni(BDC)$. The possibility of stabilizing HIPE by other MOFs was investigated. First, a one-dimensional (1D) MOF, i.e. $Mn_3(BTC)_2$ nanowire, was synthesized (Supplementary Fig. 8) and used for the emulsification of water and cyclohexane (1:1 in volume ratio). The gel-like HIPE with polyhedral cyclohexane droplets was formed (Fig. 5a,b). The cyclohexane volume fraction of the HIPE was determined to be 0.78. After extracting the solvents from HIPE, the ultralight $Mn_3(BTC)_2$ MOA with a density of $0.014 \text{ g} \cdot \text{cm}^{-3}$ was obtained (Fig. 5c). The $Mn_3(BTC)_2$ MOA presents a morphology of honeycomb structure (Fig. 5d,e). The pore shape and size are similar to those of the polyhedral droplets shown in Fig. 5b. It confirms that the $Mn_3(BTC)_2$ MOA can well preserve the structure of HIPE. From the magnified SEM image shown in Fig. 5f, it is evident that the wall of the macropore is stacked by MOF nanowires. The diameter and length of the nanowires are similar to those of the pristine $Mn_3(BTC)_2$ nanowires (Supplementary Fig. 8). The results indicate that the HIPE can conduct the reconstruction of the pre-formed MOF nanocrystals, while it has no influence on the shape and size of the MOF unit.

Further, the two-dimensional (2D) $Ni(BDC)$ ($BDC = 1,4\text{-benzenedicarboxylate}$) nanosheets were synthesized (Supplementary Fig. 9) for HIPE formation. The 2D $Ni(BDC)$ also produced the gel-like HIPE in 1:1 cyclohexane/water mixture (Fig. 5g). However, the droplets are spherical and less crowded than those in the HIPEs stabilized by $Cu_3(BTC)_2$ and $Mn_3(BTC)_2$ (Fig. 5h). It can be partly due to the lower cyclohexane volume fraction (0.73) of the HIPE stabilized by $Ni(BDC)$. Besides, due to steric repulsion effect, the 2D structure of $Ni(BDC)$ nanosheet may be unfavorable for the efficient linkage of MOF crystals to form a HIPE structure as compact as the above two HIPEs stabilized by 0D and 1D nanocrystals. The $Ni(BDC)$ MOA obtained from the HIPE (Fig. 5i) has a density of $0.012 \text{ g} \cdot \text{cm}^{-3}$. It presents a morphology of hollow spheres (Fig. 5j,k) and their sizes distribute in a similar range with the HIPE droplets shown in Fig. 5h (5–20 μm). As can be seen from the magnified SEM image shown in Fig. 5l, the wall of the hollow sphere is ultrathin and formed by the connection of nanosheets along the surface. The $Mn_3(BTC)_2$ and $Ni(BDC)$ MOAs well preserve the respective crystal forms of the pristine MOFs (Supplementary Figs 10 and 11). The above results prove that the HIPEs can be stabilized by different MOFs, which are versatile in producing MOAs with modulated structures.

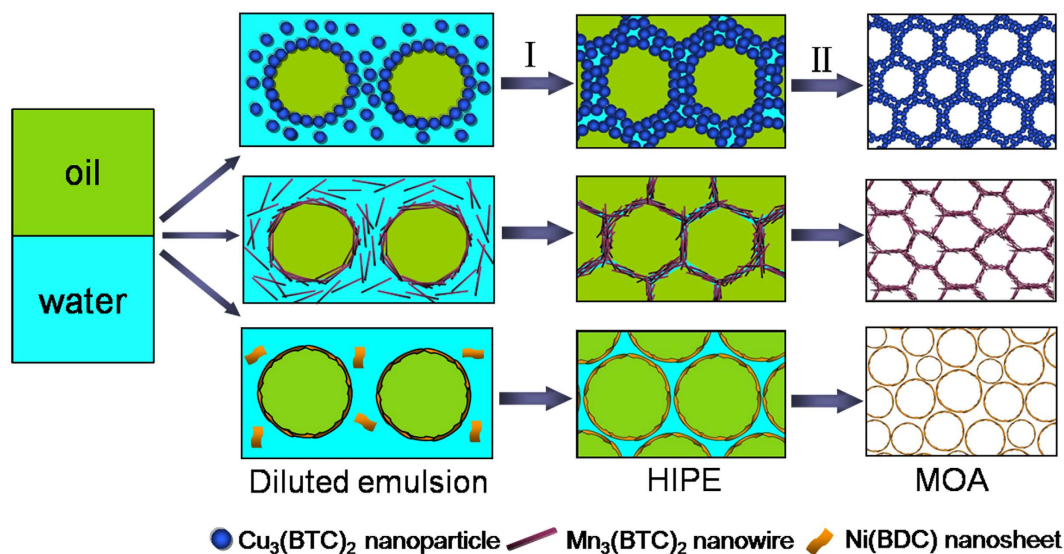


Figure 6. Diagram illustrating the process for the formation of HIEPs stabilized by different MOF nanocrystals and the derivation of MOAs. I, Separating excess water from diluted emulsion; II, removing solvents from HIPE.

Mechanism. Zeta potential is usually used to judge the hydrophilic property of particles and the electrostatic interaction among particles⁵⁰. To explore the underlying mechanism for the HIPE formation, the zeta potentials of the MOFs in water were determined. The zeta potentials of $\text{Cu}_3(\text{BTC})_2$, $\text{Mn}_3(\text{BTC})_2$ and $\text{Ni}(\text{BDC})$ in water ($1 \text{ mg}\cdot\text{mL}^{-1}$) were -0.54 mV , -2.42 mV and -0.42 mV , respectively. All the three MOFs have negative and mid-range zeta potentials, allowing suitable amphiphilicity and weak repulsions between MOF nanocrystals. Therefore, the MOF nanocrystals can be anchored at oil-water interface and emulsify the two immiscible phases (Fig. 6a). In addition to the nanocrystals adsorbed at oil-water interface, there are nanocrystals that dispersed in aqueous phase.

The diluted emulsion with a large amount of water was unstable, resulting in water sedimentation and creaming up of oil drops^{34,51}. During this process, the nanocrystals adsorbed at oil-water interface are probably contiguous with those dispersed in aqueous phase. Among the three MOFs, $\text{Mn}_3(\text{BTC})_2$ nanocrystals have the weakest electrostatic repulsion between nanocrystals in continuous phase and interfacial nanocrystals. So the $\text{Mn}_3(\text{BTC})_2$ nanocrystals from different oil droplets and continuous phase are bound together into a 3D network, which in turn traps the oil droplets in gel matrix (Fig. 6b). $\text{Cu}_3(\text{BTC})_2$ and $\text{Ni}(\text{BDC})$ have similar zeta potentials; however, the 2D nanosheet structure of $\text{Ni}(\text{BDC})$ creates a steric barrier for the effective linkage of nanocrystals into a network. Consequently, $\text{Ni}(\text{BDC})$ nanosheets are adsorbed at oil-water interface to form spherical droplets (Fig. 6b). The gel-like HIPE was much stable because the continuous phase filled with nanocrystals was highly viscous and the nanocrystals at oil-water interface can cross link into network or aggregate closely to hinder droplet coalescence⁵⁰ (Fig. 6b). After extracting the liquids, the HIEPs stabilized by $\text{Cu}_3(\text{BTC})_2$ and $\text{Mn}_3(\text{BTC})_2$ produced 3D interconnected MOAs, while the HIPE stabilized by $\text{Ni}(\text{BDC})$ favored the formation of MOA with spherical capsules (Fig. 6c).

Discussion

Here the formation of a MOF-stabilized HIPE was proposed. It was found that the MOF nanocrystals, including 0D nanoparticles, 1D nanowires and 2D nanosheets, could emulsify the two immiscible solvents (water and oil) and produce stable HIEPs. The structures of HIEPs can be easily tuned by adjusting the properties of MOF nanocrystals and oil-to-water ratio. The MOF nanocrystals assembled at oil-water interface play an exceptional role in stabilising the HIPE. In comparison with the conventional HIEPs, the MOF-stabilized HIPE has many advantages. For example, the HIPE could be prepared by stirring the mixture of water, oil and MOF at room temperature, involving no additional additives or high-energy input. Also, the functionalization for the commonly used organic or inorganic particles for HIPE formation is avoided due to the hybrid and amphiphilic property of MOF itself.

The above HIEPs with high viscosity and low MOF concentration ($<3.0 \text{ wt}\%$) endow them unique merits in producing intact and highly porous MOA monoliths. The ultralight MOA monoliths with densities as low as $0.01 \text{ g}\cdot\text{cm}^{-3}$ were obtained after extracting the liquids, which well preserve the skeleton replicas of HIEPs. It is worth noting that MOA is generally derived from a MOG matrix^{20–24}, which is often difficult due to the particle precipitation or crystallization during the gelation process. To get the desired MOG, heating for the solution of precursors ($>80^\circ\text{C}$) and aging for the wet gel up to days are usually requisite. The MOF-stabilized HIPE route is facile and can be applied to the synthesis of different kinds of MOA monoliths. We anticipate that more MOAs and MOA composites (e.g. MOA/MOA, metal/MOA, metal oxide/MOA, etc) with unique features would be prepared by the HIPE route and find applications in catalysis, adsorption and energy storage.

Methods

MOF synthesis. $\text{Cu}_3(\text{BTC})_2$ was synthesized according to literature⁴¹. Typically, $\text{Cu}(\text{OAc})_2 \cdot \text{H}_2\text{O}$ (2.0 g) and H_3BTC (1.4 g) were respectively dissolved in a 1:1 water/ethanol mixture (25 mL). Then the two solutions were mixed and stirred rapidly for 1 h. The precipitate was centrifugated, washed with ethanol and dried under vacuum. For the synthesis of $\text{Mn}_3(\text{BTC})_2$, MnCl_2 (1.89 g) and H_3BTC (2.1 g) were mixed with 50 mL ethanol under vigorous agitation. 2 mL triethylamine was added into the above solution at room temperature. After reaction for 6 hrs, the white precipitate was washed with ethanol and dried at 60 °C under vacuum for 24 hrs. For the synthesis of $\text{Ni}(\text{BDC})$, $\text{NiCl}_2 \cdot 6\text{H}_2\text{O}$ (1.5 g) and H_2BDC (2.0 g) were added into ethanol (50 mL), the other experimental procedures and conditions being the same as those for the $\text{Mn}_3(\text{BTC})_2$ synthesis.

Emulsion formation and characterization. The desired amount of MOF was added into the water-oil mixture with a certain oil volume fraction and the mixture was stirred at room temperature for 3 hrs. The MOF concentration was fixed at 10 mg·mL⁻¹ of the overall emulsion volume. Then the mixture was kept without agitation to allow phase separation. The lower water was removed by injector and the upper HIPE was characterized by OLYMPUS FV1000-IX81 confocal laser scanning microscopy with excitation wavelength of 559 nm. 5.0 μL emulsion containing Rhodamine B (10⁻⁴ M) was trickled on a 0.7 mm thick cover slip through microsyringe and covered with another, and was monitored and captured by a digital CCD.

MOA formation and characterization. The as-prepared HIPE was first treated by supercritical CO₂ to remove oil and then frozen at -20 °C for 2 hrs. CO₂ was released slowly and the sample was lyophilized for 20 hrs to remove water. Then the product was obtained. The morphologies of the MOAs were characterized by scanning electron microscope (SEM, HITACHI S-4800). XRD was performed on a Rigaku D/max-2500 diffractometer with Cu Kα radiation ($\lambda = 1.5418 \text{ \AA}$) at 40 kV and 200 mA. The macroporosities were recorded by mercury intrusion porosimetry using a Micromeritics Autopore IV 9500 porosimeter. The sample was subjected to a pressure cycle starting at 5 psia, increasing to 44500 psia in predefined steps to give pore size/pore volume information. N₂ adsorption-desorption isotherms were obtained using a Micromeritics ASAP 2020M system. The FT-IR spectra were obtained using a Bruker Tensor 27 spectrometer. Malvern Zetasizer Nano-ZS instrument (ZEN3600, Malvern Instruments, Worcestershire, UK), equipped with a 4 mW He-Ne laser (wavelength 633 nm), was used to determine zeta potential of the MOF mixed with water. The concentration of MOF suspension was fixed at 1 mg·mL⁻¹ and the measurement was conducted at 25.0 ± 0.1 °C. The compression test was carried out using a model 3342 Instron Universal Testing Machine at a rate of 20% strain min⁻¹.

Adsorption performance of MOA. The test was carried out by continuously shaking the mixture of 10 mL dye aqueous solution (100 mg L⁻¹) with the MOA or MOF (10 mg) for different times. After centrifuging, the dye concentration was analyzed using a Shimadzu UV-2450 UV-vis spectrophotometer. For the gas adsorption test, the adsorption isotherms of CO₂, N₂ and CH₄ were recorded at 273.2 K for MOAs and pristine MOF in pressure range of 0.0004–1 atm on a TriStar II 3020 device. For each measurement, about 100 mg of the sample was degassed using the same procedure.

References

- Furukawa, H., Müller, U. & Yaghi, O. M. "Heterogeneity within Order" in metal-organic frameworks. *Angew. Chem. Int. Ed.* **54**, 3417–3430 (2015).
- Furukawa, H., Cordova, K. E., O'Keeffe, M. & Yaghi, O. M. The chemistry and applications of metal-organic frameworks. *Science* **341**, 1230444 (2013).
- Burtch, N. C., Jasuja, H. & Walton, K. S. Water Stability and Adsorption in metal-organic frameworks. *Chem. Rev.* **114**, 10575–10612 (2014).
- Murray, L. J., Dincă, M. & Long, J. R. Hydrogen storage in metal-organic frameworks. *Chem. Soc. Rev.* **38**, 1294–1314 (2009).
- Makal, T. A., Li, J.-R., Lua, W. & Zhou, H.-C. Methane storage in advanced porous materials. *Chem. Soc. Rev.* **41**, 7761–7779 (2012).
- He, Y., Zhou, W., Qian, G. & Chen, B. Methane storage in metal-organic frameworks. *Chem. Soc. Rev.* **43**, 5657–5678 (2014).
- Yan, Y., Yang, S., Blake, A. J. & Schröder, M. Studies on metal-organic frameworks of Cu(II) with isophthalate linkers for hydrogen storage. *Acc. Chem. Res.* **47**, 296–307 (2014).
- Li, J.-R., Kuppler, R. J. & Zhou, H.-C. Selective gas adsorption and separation in metal-organic frameworks. *Chem. Soc. Rev.* **38**, 1477–1504 (2009).
- Voorde, B. V., Bueken, B., Denayer, J. & Vos, D. D. Adsorptive separation on metal-organic frameworks in the liquid phase. *Chem. Soc. Rev.* **43**, 5766–5788 (2014).
- Li, J.-R., Sculley, J. & Zhou, H.-C. Metal-organic frameworks for separations. *Chem. Rev.* **112**, 869–932 (2012).
- Douvali, A. *et al.* Turn-on luminescence sensing and real-time detection of traces of water in organic solvents by a flexible metal-organic framework. *Angew. Chem. Int. Ed.* **54**, 1651–1656 (2015).
- Gassensmith, J. J. *et al.* A Metal-organic framework-based material for electrochemical sensing of carbon dioxide. *J. Am. Chem. Soc.* **136**, 8277–8282 (2014).
- Zhang, M. *et al.* Two-dimensional metal-organic framework with wide channels and responsive turn-on fluorescence for the chemical sensing of volatile organic compounds. *J. Am. Chem. Soc.* **136**, 7241–7244 (2014).
- Campbell, M. G., Sheberla, D., Liu, S. F., Swager, T. M. & Dinca, M. $\text{Cu}_3(\text{hexaiminotriphenylene})_2$: An electrically conductive 2D metal-organic framework for chemiresistive sensing. *Angew. Chem. Int. Ed.* **54**, 4349–4352 (2015).
- Corma, A., García, H. & Llabrés i Xamena & F. X. Engineering metal organic frameworks for heterogeneous catalysis. *Chem. Rev.* **110**, 4606–4655 (2010).
- Dhakshinamoorthy, A. & Garcia, H. Catalysis by metal nanoparticles embedded on metal-organic frameworks. *Chem. Soc. Rev.* **41**, 5262–5284 (2012).
- Falkowski, J. M. *et al.* Privileged Phosphine-based metal-organic frameworks for broad-scope asymmetric catalysis. *J. Am. Chem. Soc.* **136**, 5213–5216 (2014).
- Dhakshinamoorthy, A., Asiric, A. M. & Garcia, H. Metal-organic frameworks catalyzed C-C and C-heteroatom coupling reactions. *Chem. Soc. Rev.* **44**, 1922–1947 (2015).
- Manna, K., Zhang, T., Greene, F. X. & Lin, W. Bipyridine- and phenanthroline-based metal-organic frameworks for highly efficient and tandem catalytic organic transformations via directed C-H activation. *J. Am. Chem. Soc.* **137**, 2665–2673 (2015).

20. Lohe, M. R., Rose, M. & Kaskel, S. Metal-organic framework (MOF) aerogels with high micro- and macroporosity. *Chem. Commun.* **40**, 6056–6058 (2009).
21. Li, L. *et al.* A synthetic route to ultralight hierarchically micro/mesoporous Al(III)-carboxylate metal-organic aerogels. *Nat. Commun.* **4**, 1774 (2013).
22. Xia, W. *et al.* Facile and economical synthesis of metal-organic framework MIL-100(Al) gels for high efficiency removal of microcystin-LR. *RSC Adv.* **3**, 11007–11013 (2013).
23. Li, H. *et al.* Luminescent metal-organic gels with tetraphenylethylene moieties: Porosity and aggregation-induced emission. *RSC Adv.* **3**, 16340–16344 (2013).
24. Piepenbrock, M. O. M., Lloyd, G. O., Clarke, N. & Steed, J. W. Metal- and anion-binding supramolecular gels. *Chem. Rev.* **110**, 1960–2004 (2010).
25. Butler, R., Hopkinson, I. & Cooper, A. I. Synthesis of porous emulsion-templated polymers using high internal phase CO₂-in-water emulsions. *J. Am. Chem. Soc.* **125**, 14473–14481 (2003).
26. Schüler, F. *et al.* Synthesis of macroporous polystyrene by the polymerization of foamed emulsions. *Angew. Chem. Int. Ed.* **51**, 2213–2217 (2012).
27. Oschatz, M. *et al.* Carbide-derived carbon monoliths with hierarchical pore architectures. *Angew. Chem. Int. Ed.* **51**, 7577–7580 (2012).
28. Zhang, H. F. & Cooper, A. I. Synthesis and applications of emulsion-templated porous materials. *Soft Matter* **1**, 107–113 (2005).
29. Dhanuka, V. V., Dickson, J. L., Ryo, W. & Johnston, K. P. High internal phase CO₂-in-water emulsions stabilized with a branched nonionic hydrocarbon surfactant. *J. Colloid Interface Sci.* **298**, 406–418 (2006).
30. Ikem, V. O., Menner, A. & Bismarck, A. High internal phase emulsions stabilized solely by functionalized silica particles. *Angew. Chem. Int. Ed.* **47**, 8277–8279 (2008).
31. Li, Z., Ming, T., Wang, J. & Ngai, T. High internal phase emulsions stabilized solely by microgel particles. *Angew. Chem. Int. Ed.* **45**, 8490–8493 (2009).
32. Sun, G., Li, Z. & Ngai, T. Inversion of particle-stabilized emulsions to form high-internal-phase emulsions. *Angew. Chem. Int. Ed.* **49**, 2163–2166 (2010).
33. Huo, J., Marcello, M., Garai, A. & Bradshaw, D. MOF-polymer composite microcapsules derived from pickering emulsions. *Adv. Mater.* **25**, 2717–2722 (2013).
34. Xiao, B., Yuan, Q. & Williams, R. A. Exceptional function of nanoporous metal organic framework particles in emulsion stabilization. *Chem. Commun.* **49**, 8208–8210 (2013).
35. Chui, S. S. Y., Lo, S. M. F., Charmant, J. P. H., Orpen, A. G. & Williams, I. D. A chemically functionalizable nanoporous material [Cu₃(TMA)₂(H₂O)₃]_n. *Science* **283**, 1148–1150 (1999).
36. Qiu, L.-G. *et al.* Hierarchically micro- and mesoporous metal-organic frameworks with tunable porosity. *Angew. Chem. Int. Ed.* **47**, 9487–9491 (2008).
37. Xiang, S., Zhou, W., Gallegos, J. M., Liu, Y. & Chen, B., Exceptionally high acetylene uptake in a microporous metal-organic framework with open metal sites. *J. Am. Chem. Soc.* **131**, 12415–12419 (2009).
38. Sun, L.-B., Li, J.-R., Park, J. & Zhou, H.-C. Cooperative template-directed assembly of mesoporous metal-organic frameworks. *J. Am. Chem. Soc.* **134**, 126–129 (2012).
39. Peng, L. *et al.* Surfactant-directed assembly of mesoporous metal-organic framework nanoplates in ionic liquids. *Chem. Commun.* **48**, 8688–8690 (2012).
40. Peng, L. *et al.* Highly mesoporous metal-organic framework assembled in a switchable solvent. *Nat. Commun.* **5**, 5465 (2014).
41. Zhang, B. *et al.* Solvent determines the formation and properties of metal-organic frameworks. *RSC Adv.* **5**, 37691–37696 (2015).
42. Li, J., Zhang, J., Zhao, Y., Han, B. & Yang, G. High-internal-ionic liquid-phase emulsions. *Chem. Commun.* **48**, 994–996 (2012).
43. Zhang, D. & Clegg, P. S. Relationship between high internal-phase Pickering emulsions and catastrophic inversion. *Soft Matter* **9**, 7042–7048 (2013).
44. Lee, K.-Y., Blaker, J. J., Murakami, R., Heng, J. Y. Y. & Bismarck, A. Phase behavior of medium and high internal phase water-in-oil emulsions stabilized solely by hydrophobized bacterial cellulose nanofibrils. *Langmuir* **30**, 452–460 (2014).
45. Zheng, X., Zhang, Y., Wang, H. & Du, Q. Interconnected macroporous polymers synthesized from silica particle stabilized high internal phase emulsions. *Macromolecules* **47**, 6847–6855 (2014).
46. Ahmed, A., Forster, M., Clowes, R., Myers, P. & Zhang, H. F. Hierarchical porous metal-organic framework monoliths. *Chem. Commun.* **50**, 14314–14316 (2014).
47. Moitra, N. *et al.* Mechanically stable, hierarchically porous Cu₃(btc)₂ (HKUST-1) monoliths via direct conversion of copper(II) hydroxide-based monoliths. *Chem. Commun.* **51**, 3511–3514 (2015).
48. Xiang, S. L. *et al.* Porous organic-inorganic hybrid aerogels based on Cr³⁺/Fe³⁺ and rigid bridging carboxylates. *J. Mater. Chem. A.* **22**, 1862–1867 (2012).
49. Lin, S. *et al.* Adsorption behavior of metal-organic frameworks for methylene blue from aqueous solution. *Micropor. Mesopor. Mater.* **193**, 27–34 (2014).
50. Tan, H. *et al.* Gelatin particle-stabilized high internal phase emulsions as nutraceutical containers. *ACS Appl. Mater. Interfaces* **6**, 13977–13984 (2014).
51. Aveyard, R., Binks, B. P. & Clint, J. H. Emulsions stabilised solely by colloidal particles. *Adv. Colloid Interface Sci.* **503**, 100–102 (2003).

Acknowledgements

We thank the National Natural Science Foundation of China (21525316, 21173238, 21133009, U1232203, 21021003), Chinese Academy of Sciences (KJCX2.YW.H16).

Author Contributions

B.X. Zhang performed the whole experiments. C.C., Liu, L. Peng and X.X. Sang worked on the MOF characterization. X. Ma, T. Luo, X.N. Tan and G.Y. Yang worked on the adsorption determination. B.X. Zhang, J.L. Zhang and B.X. Han analyzed the data and proposed the mechanism. J.L. Zhang and B.X. Zhang wrote the text. J.L. Zhang conceived the project and designed the experiments.

Additional Information

Supplementary information accompanies this paper at <http://www.nature.com/srep>

Competing financial interests: The authors declare no competing financial interests.

How to cite this article: Zhang, B. *et al.* High-internal-phase emulsions stabilized by metal-organic frameworks and derivation of ultralight metal-organic aerogels. *Sci. Rep.* **6**, 21401; doi: 10.1038/srep21401 (2016).



This work is licensed under a Creative Commons Attribution 4.0 International License. The images or other third party material in this article are included in the article's Creative Commons license, unless indicated otherwise in the credit line; if the material is not included under the Creative Commons license, users will need to obtain permission from the license holder to reproduce the material. To view a copy of this license, visit <http://creativecommons.org/licenses/by/4.0/>